Computers in Biology and Medicine 108 (2019) 249–262

Contents lists available at ScienceDirect

Computers in Biology and Medicine

journal homepage: www.elsevier.com/locate/compbiomed

Dynamic coherence factor based on the standard deviation for coherent plane-wave compounding

Yadan Wang, Chichao Zheng*, Hu Peng

Department of Biomedical Engineering, Hefei University of Technology, Hefei, 230009, China

ARTICLE INFO

Keywords:
Ultrasound imaging
Coherent plane-wave compounding
Coherence factor
Dynamic coherence factor
Standard deviation
Square neighborhood

ABSTRACT

The ultrafast imaging technique based on plane wave transmission has been a commonly investigated imaging mode in medical ultrasound imaging. Coherent plane-wave compounding (CPWC) was proposed to improve the quality of plane-wave imaging (PWI), which obtained a high-quality image by summing the low-quality images formed by transmitting plane waves at different steering angles. Coherence factor (CF) weighting algorithms can effectively improve image contrast with low computational complexity. However, this usually introduces black artifacts and degraded speckle quality. In this paper, we propose a dynamic coherence factor (DCF) that is based on the angular difference of CPWC to adaptively determine the number of plane waves and utilizes several plane waves with small angular difference to evaluate coherence. To improve resolution and contrast-to-noise ratio (CNR), adjusted DCF (ADCF) introduces a parameter related to the standard deviation to adjust DCF. Furthermore, a square neighborhood ADCF (SN-ADCF) using a 2-dimensional average filter is designed to obtain higher contrast and speckle quality. The simulated, experimental and *in-vivo* datasets are used to evaluate the proposed methods. Results show that, in comparison with CF, DCF can achieve improved contrast ratio (CR), CNR and speckle signal-to-noise ratio (sSNR). ADCF achieves a maximal lateral full width at half maximum (FWHM) improvement by 40% and better speckle quality than CF. SN-ADCF causes about 20% improvements upon CF in CNR and sSNR, while maintaining a similar resolution performance. SN-ADCF also provides higher lateral resolution than the generalized coherence factor (GCF) and scaled coherence factor (scCF), meanwhile obtaining a comparable contrast and speckle quality. Therefore, SN-ADCF has a satisfying comprehensive performance, which can achieve a reasonable balance among resolution, contrast and speckle quality.

1. Introduction

Ultrasound imaging is a major medical imaging modality in the field of medical imaging and has been widely used in clinical examination and diagnostics. Conventional B-mode imaging requires multiple emission focusing to scan the imaging region, which leads to a low frame rate. With the development of imaging techniques such as functional brain imaging, real-time 3-D imaging and real-time elastography, traditional B-mode imaging can hardly satisfy the requirement of high frame rates. Ultrasound plane-wave imaging (PWI) allows for ultrafast image acquisition rates. Thus, it has been extensively applied to medical ultrasound imaging [1,2]. Despite the high frame rate, PWI usually has a low image quality caused by the lack of focusing in the process of pulse emission [3,4]. Lu developed a high frame rate imaging theory and extended it through the use of spatial compounding with different steered plane waves or limited diffraction beams [5–7]. Images reconstructed with different steering angles can be combined in a coherent way (enhancing resolution) or incoherent way (reducing speckle) [5,6]. Montaldo et al. [8] proposed coherent plane-wave compounding (CPWC) based on the coherent summation of the echo data obtained from plane-wave transmission at different angles in the time-space domain, which could achieve a trade-off between the frame rate and image quality. These authors show that the CPWC approach performs as well as the optimal multifocus image with a significantly higher frame rate. Follow-up studies found that CPWC had a good performance in various applications [9], such as blood or tissue motion estimation [10,11], shear wave elasticity imaging [12,13] and parametric imaging [14]. Though CPWC obtains a higher image quality than PWI and conventional focus ultrasound imaging, it suffers from a limited resolution and poor contrast performance due to the use of the nonadaptive delay-and-sum (DAS) beamforming.

Adaptive beamforming techniques are effective and common methods forthe reconstruction of high-quality images. Coherence-based beamformers are a major category, which shows the capability of noise

* Corresponding author.
E-mail address: cczheng@hfut.edu.cn (C. Zheng).

https://doi.org/10.1016/j.compbiomed.2019.03.022
Received 26 November 2018; Received in revised form 22 March 2019; Accepted 23 March 2019

suppression and contrast enhancement [15]. Coherence factor (CF) is defined as the ratio between coherent and incoherent energy in the received signals across an aperture. When used as a weighting factor, CF has a good aberration reduction and sidelobe suppression activities [16]. However, CF introduces image artifacts when the signal-to-noise ratio (SNR) is low [17]. Therefore, several extensions of CF were developed to improve stability [17–19]. A spatial frequency-domain version of CF, named generalized coherence factor (GCF), was proposed in Ref. [18] to reduce focusing errors resulting from the sound-velocity inhomogeneities, which is also an index of the focusing quality and can be used as a weighting factor for the reconstructed image. Camacho et al. [19] devised the phase coherence factor (PCF) and the sign coherence factor (SCF) based on the dispersion of phases to weight the coherent sum output for grating and sidelobe suppression in ultrasound imaging. Nilsen and Holm [17] showed how the CF could be interpreted as a Wiener postfilter that puts too much emphasis on the incoherent noise of the sensors. This is the reason why CF will underestimate the magnitude of scatters and overcompensate for the sidelobe effects in the immediate area surrounding the cyst in low-SNR cases. Compared to CF, the scaled Wiener postfilter (ScW) provides better robustness, fewer artifacts and enhanced contrast.

Though these efforts have been made for ultrasound imaging to modify CF, the above beamforming methods might be limited to certain imaging modalities. Therefore, researchers have studied modified CF methods for specific imaging modes. High-frame-rate imaging and photoacoustic imaging often suffer from a low SNR because of the unfocused acoustic beam and limited laser energy. The CF method is generally difficult to separate noise from sidelobes. Thus, it over-suppresses desired signals and decreases the image intensity. SNR-dependent CF was proposed for high-frame-rate and photoacoustic imaging to overcome this problem [20], which takes into account the local SNR to maintain the desired signal level but reduce the unwanted noise when SNR is low. Eigenspace-based coherence factor (ESBCF), which combines the information from signal eigenspace and coherence factor by expanding the CF to the covariance matrix of the signal, was proposed to enhance the contrast ratio and maintain the high resolution of the tissue harmonic imaging [21]. Mozaffarzadeh et al. [22] used the output of DMAS algorithm instead of the DAS on the numerator of the CF formula to obtain the modified CF (MCF) for photoacoustic imaging. Experimental results have shown that MCF can lead to resolution and sSNR improvement.

CPWC utilizes plane waves that are transmitted at multiple steering angles to reconstruct images. Thus, it should be considered that the spatial coherence properties and angular difference of backscattered signals at different transmit angles may impact on the image quality. Li and Dahl [23] studied the angular coherence in ultrasound imaging, in which the results showed that the angular coherence of plane-wave imaging results decreases as the angular spacing increases. Some beamformers have been studied to reject less coherent signals based on the angular coherence [24–27]. Guo et al. [24] proposed a global effective distance-based sidelobe suppressing method for CPWC with a limited frame number. An approach using two uniform angle sets with different intervals to generate a non-uniformly distributed plane-wave angle set was presented for grating lobe level reduction [25]. The eigenspace generalized sidelobe canceller (EGSC) beamformer combined with an SNR-dependent CF is suggested for CPWC imaging [26]. To suppress the sidelobes and clutter in CPWC imaging, an angle coherence factor (ACF) was proposed and introduced to CPWC [27]. Results demonstrated that ACF greatly suppressed the sidelobes while keeping equivalent lateral resolution and contrast compared with CPWC.

Our study aims at modifying CF methods based on the particular characteristic of CPWC for high quality images. This paper studies the adaptive weighting techniques combining with the angular difference for CPWC to suppress sidelobes and reduce noise. A dynamic coherence factor (DCF) for CPWC is put forward, which is based on the angular difference and noise variation to modify the CF. DCF utilizes several plane-wave imaging results with a small angular difference to calculate the weighting factor, and it can more accurately evaluate the signal coherence. To improve the resolution and speckle quality of DCF, we introduce the dynamic coherence factor adjusted by normalized standard deviation, named adjusted dynamic coherence factor (ADCF). In CPWC, a spatial sequence consisting of every steered plane-wave imaging result can be constituted for every imaging point. Then, the normalized standard deviation is obtained by normalizing the standard deviations of all the spatial sequences. Furthermore, a square neighborhood ADCF (SN-ADCF) is designed to further enhance the image quality in contrast and speckle. The proposed three methods were tested on the International Ultrasonics Symposium (IUS) 2016 beamforming challenge datasets [28,29]. CF, GCF and scaled coherent factor (scCF) are also presented to compare with the proposed methods. Simulation, experimental phantom and *in-vivo* results show that the proposed methods can provide higher contrast-to-noise ratio (CNR) and speckle signal-to-noise ratio (sSNR) than CF, while achieving good contrast ratio (CR) and resolution performance. In the proposed methods, SN-ADCF can achieve a good balance among the resolution, contrast and speckle quality. SN-ADCF provides improved lateral resolution and contrast compared with GCF, and shows better resolution and similar contrast and speckle quality compared with scCF.

The rest of this paper is organized as follows: In Section 2, the CPWC, CF, GCF, scCF and the proposed methods are respectively introduced. The simulation and experimental materials are presented in Section 3. The simulation and experimental results are presented in Section 4. Discussions on the proposed methods are given in Section 5. Finally, a conclusion is drawn in Section 6.

2. Method

2.1. Coherent plane wave compounding

To generate a compounded image, multiple plane-wave images are obtained by transmitting plane waves with different steering angles. When the i-th plane-wave steered at an angle α_i is emitted, the time to go to an imaging point $p(x_p, z_p)$ is:

$$\tau_i = (z_p \cos\alpha_i + x_p \sin\alpha_i)/c_0 \tag{1}$$

where c_0 is the speed of sound in the medium. The time to come back to a transducer placed in x_r is:

$$\tau_r = \frac{1}{c_0}\sqrt{(x_p - x_r)^2 + z_p^2} \tag{2}$$

Then, the beamforming result of PWI at imaging point p is given by:

$$y(p, \alpha_i) = \sum_{r=1}^{M} u(x_r) h_{i,r}(\tau_i + \tau_r) \tag{3}$$

where M is the number of elements in the transducer, and $h_{i,r}$ is defined as the signal received by element located at x_r. $u(x_r)$ represents the receive apodization windows and this paper uses a tapered 25% Tukey window.

The output of CPWC at point p is expressed as:

$$Y_{CPWC}(p) = \frac{1}{2N+1} \sum_{i=-N}^{N} y(p, \alpha_i) \tag{4}$$

where $(2N + 1)$ is the total number of angles.

2.2. Coherence factor for CPWC

In the multi-angle plane-waves compounding, for an imaging point p, a spatial signal sequence can be established after every steered plane-wave beamforming. $Y_p = [y(p, \alpha_{-N}), y(p, \alpha_{-N+1}), \cdots, y(p, \alpha_N)]$ is assumed as the sequence at point p. CF is defined as the ratio of coherent

energy and incoherent energy. The CF can be expressed as:

$$CF(p) = \frac{|\sum_{i=-N}^{N} y(p, \alpha_i)|^2}{(2N+1)\sum_{i=-N}^{N} |y(p, \alpha_i)|^2} \tag{5}$$

Then, the expression of CF weighted CPWC can be given by:

$$Y_{CF}(p) = CF(p) \times Y_{CPWC}(p) \tag{6}$$

2.3. Generalized coherence factor for CPWC

GCF is defined as the ratio of the spectral energy within a pre-specified low-frequency region to the total energy. GCF is formulated by:

$$GCF(p) = \frac{\sum_{k \in \text{low-frequency region}} |P(k)|^2}{\sum_{k=1}^{2N+1} |P(k)|^2} \tag{7}$$

where $P(k)$ is the spectrum of the sequence Y_p, and $2N+1$ is the number of points in the discrete spectrum, which is equal to the number of plane waves. The low-frequency region is specified by a cutoff frequency M_0 in the spatial frequency index (i.e. from $-M_0$ to M_0). The effects of M_0 values on the resolution, CR and CNR have been analyzed in Ref. [18]. According to the analysis, M_0 is set as 1 for GCF in this paper.

The expression of GCF weighted CPWC can be given by:

$$Y_{GCF}(p) = GCF(p) \times Y_{CPWC}(p) \tag{8}$$

2.4. Scaled coherence factor for CPWC

The scCF is an SNR-dependent CF, which takes into account the local SNR in the CF formulation so that the contrast can be restored when the SNR is low [20]. It used the coherent and incoherent energy and did not need to know the noise power in the output [4]. The scCF is formulated as:

$$scCF(p) = \frac{CF(p)}{CF(p) + \eta(SNR)(1 - CF(p))} \tag{9}$$

The coefficient $\eta(SNR) = \eta(P_s, P_n)$ is determined by using a sigmoid function of the SNR, which is calculated by:

$$\eta(P_s, P_n) = \frac{N-1}{2N}\left\{1 - \tanh\left[\alpha\left(\frac{P_s}{P_n} - \beta\right)\right]\right\} + \frac{1}{N} \tag{10}$$

where P_s (the power within the frequency range from $-M_0$ to M_0) indicates the signal power, and P_n (the power other than the signal power) represents the noise power. In this work, we simply use the parameters P_s, P_n, α and β in the way same as in Ref. [20]. The DC component ($M_0 = 0$) is used for P_s and the rest of the frequency components are averaged to estimate the noise level P_n. Values of 1 and π are chosen for parameters α and β, respectively. The local SNRs are averaged for one wavelength to improve the robustness.

Accordingly, scCF weighted CPWC is expressed by:

$$Y_{scCF}(p) = scCF(p) \times Y_{CPWC}(p) \tag{11}$$

2.5. Dynamic coherence factor for CPWC

In this section, the dynamic coherence factor (DCF) is presented as an adaptive weighting factor for CPWC. In plane wave imaging, deeper regions often suffer from a lower SNR. CF displays high sensitivity to SNR, and it always overestimates the coherent signal. This will cause an underestimation of speckle magnitude and lead to a worse speckle quality at a deeper region. The SNR difference in various depth regions can be reflected by the standard deviation variation of echo signals. DCF is thus proposed to evaluate the signal coherence more accurately based on standard deviation. The standard deviation $\sigma(p)$ of Y_p is calculated by:

$$\sigma(p) = \sqrt{\frac{1}{2N+1}\sum_{i=-N}^{N} (y(p, \alpha_i) - \bar{\mu}(p))^2} \tag{12}$$

where $\bar{\mu}(p)$ is the average of the sequence Y_p. We put forward a normalized standard deviation σ', which is obtained by calculating the standard deviation values for all imaging points and normalizing the standard deviation matrix. σ' is related to the coherence and noise intensity of echo signals. To accurately estimate the signal coherence and suppress noise, a wide aperture should be selected for the high coherence signal, and a relatively narrow aperture should be selected for the low coherence signal. Thus, a parameter δ is introduced based on σ' to adaptively determine the effective plane-wave number for coherence factor calculation. At the imaging point p, $\delta(p)$ is given by:

$$\delta(p) = (1 - \sigma'(p))^2 \tag{13}$$

According to δ, DCF selects R steered plane waves with the transmitting angles closest to 0° to evaluate signal coherence, where R values are integers. $R(p)$ is defined as:

$$R(p) = \begin{cases} 2, & \text{if} \quad \delta(p) \times (2N+1)/2 < 2 \\ \lfloor \delta(p) \times (2N+1)/2 \rfloor, & \text{else} \end{cases} \tag{14}$$

As δ is between 0 and 1, we define that R ranges from 2 to N to achieve a reasonable compounding number. This means that R is set to 2 when the calculated R value is less than 2. Then, the DCF value and the output of DCF weighted CPWC at the imaging point p are respectively calculated as:

$$DCF(p) = \frac{|\sum_{i=-R(p)}^{R(p)} y(p, \alpha_i)|^2}{(2R(p)+1)\sum_{i=-R(p)}^{R(p)} |y(p, \alpha_i)|^2} \tag{15}$$

$$Y_{DCF}(p) = DCF(p) \times Y_{CPWC}(p) \tag{16}$$

2.6. Adjusted dynamic coherence factor for CPWC

From Eq. (15), DCF is actually a dynamically modifying CF. Due to its more accurate estimation of signal coherence, DCF can achieve enhanced contrast compared to CF. However, the resolution performance of DCF will be weakened because of decreasing the numbers of plane waves. DCF does not modify the calculation principle of CF. It will have limited ability to improve the performance of CF. Adjusted DCF (ADCF) utilizing the parameter δ to adjust DCF is proposed for the resolution improvement and the speckle quality enhancement. ADCF can be expressed as:

$$ADCF(p) = \delta(p) \times DCF(p) \tag{17}$$

The incoherent signals contain desired signals which should be preserved to be used for beamforming images. However, CF over-suppresses the desired signals leading to dark artifacts in the speckle region. The normalized standard deviation σ' is closely related to the incoherence component of signals. From Eq. (13), δ is determined by σ'. Thus, δ can reflect the signal incoherence. δ Typically increases with decreasing incoherence and it decreases as the incoherence increases. ADCF using δ to multiply DCF can adjust the performance of suppressing incoherent signals and preserve desired signals. The output of ADCF weighted CPWC is given by:

$$Y_{ADCF}(p) = ADCF(p) \times Y_{CPWC}(p) \tag{18}$$

2.7. Square neighborhood adjusted dynamic coherence factor for CPWC

To further enhance the contrast and speckle quality, SN-ADCF introduces a 2-dimensional moving average filter to calculate the square neighborhood average of ADCF values to weight CPWC [30]. It is

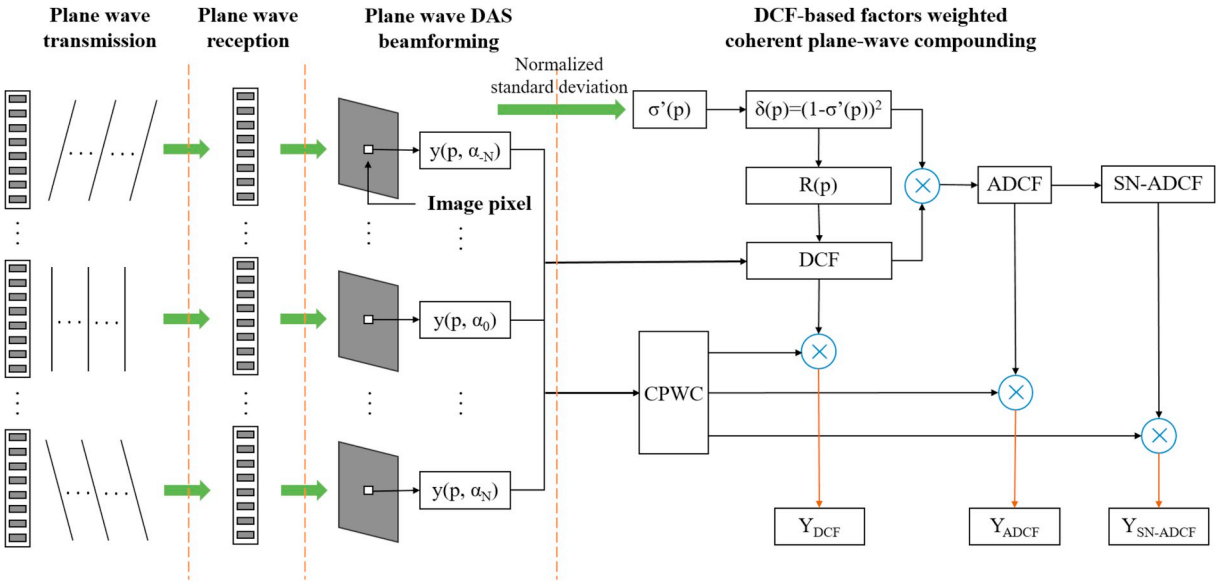

Fig. 1. The schematic diagram of the proposed methods.

expressed as:

$$SN-ADCF(p)=\frac{1}{(2S+1)(2L+1)}\sum_{s=-S}^{S}\sum_{l=-L}^{L}ADCF(z_p+s\times\Delta z,\ x_p+l\times\Delta x) \tag{19}$$

where z_p and x_p are the axial and lateral coordinates of the imaging point p, respectively. Δz and Δx are the axial pixel pitch and lateral pixel pitch, respectively. Typically, S and L are integers, which meets the condition that $(2S\times\Delta z)$ and $(2L\times\Delta x)$ are respectively equal to a transmit pulse length and one wavelength. The output of SN-ADCF weighted CPWC is given by:

$$Y_{SN-ADCF}(p)=SN-ADCF(p)\times Y_{CPWC}(p) \tag{20}$$

The schematic diagram of the proposed methods is shown in Fig. 1. First, to transmit plane waves tilted with different angles, every element transmitted ultrasound waves with different delay times. Full aperture elements were used on receive for each transmission simultaneously. Secondly, low quality images were constructed by DAS beamforming. Then, a standard deviation matrix for all image pixels can be calculated, which was used to compute the normalized standard deviation σ'. Based on σ', the DCF, ADCF and SN-ADCF could be obtained and used to weight CPWC. After the normalization and log compression, the image formation was completed for visualization.

3. Simulation and experimental setup

3.1. Simulated and experimental data

The datasets were provided by IUS 2016 beamforming challenge. Each dataset contained 75 steered plane-waves covering angles which are linearly spaced in the angle range of [– 16°, 16°] with an increment of 0.43°. The simulated datasets were generated with Field II [31,32]. The parameters used in the simulation, shown in Table 1, were set to correspond to the experimental setup [28]. The datasets containing two simulated and two experimental datasets in RF format were chosen to evaluate the proposed method. Dynamic receive aperture was used in every plane-wave beamforming procedure and the f-number is 1.75. A Gaussian distributed noise with a signal-to-noise of 10 dB was added to the simulated and experimental datasets. Beamforming images were generated using data from all 75 steering angles. The generated images have a pixel size of 0.0739 mm (axial) × 0.0986 mm (lateral).

Table 1
Imaging parameters used both in simulations and experiments.

Parameter	Value
Pitch	0.3 mm
Element width	0.27 mm
Element height	5 mm
Elevation focus	20 mm
Number of elements	128
Aperture width	38.4 mm
Transmit frequency	5.208 MHz
Sampling frequency	20.832 MHz
Pulse bandwidth	67%
Excitation	2.5 cycle
f-number	1.75

3.2. Image quality metrics

The proposed methods were compared with CPWC and CF in terms of image resolution, CR, CNR and sSNR. For point targets, the full width at half maximum (FWHM, −6 dB beam width of the mainlobe) was used as the quantitative indicator of the mainlobe width to evaluate resolution both in axial and lateral directions [33,34]. For cyst images, CR, CNR and sSNR were used to assess the performance of different imaging methods on cyst. The three ratios are defined by Refs. [35,36].

$$\mathrm{CR}=\left|20\log_{10}\left(\frac{\mu_i}{\mu_b}\right)\right| \tag{21}$$

$$\mathrm{CNR}=\frac{|\mu_i-\mu_b|}{\sqrt{\sigma_i^2+\sigma_b^2}} \tag{22}$$

$$\mathrm{sSNR}=\frac{\mu_b}{\sigma_b} \tag{23}$$

where μ_i and μ_b are the mean values inside the cyst target and in the speckle background, respectively. Inside the cyst means inside the red circle in Fig. 4(a) and Fig. 8(a), and in the speckle background means within the two green circles. σ_i and σ_b are the corresponding standard deviations. The parameters μ_i, μ_b, σ_i and σ_b are calculated before log compression and without envelope detection.

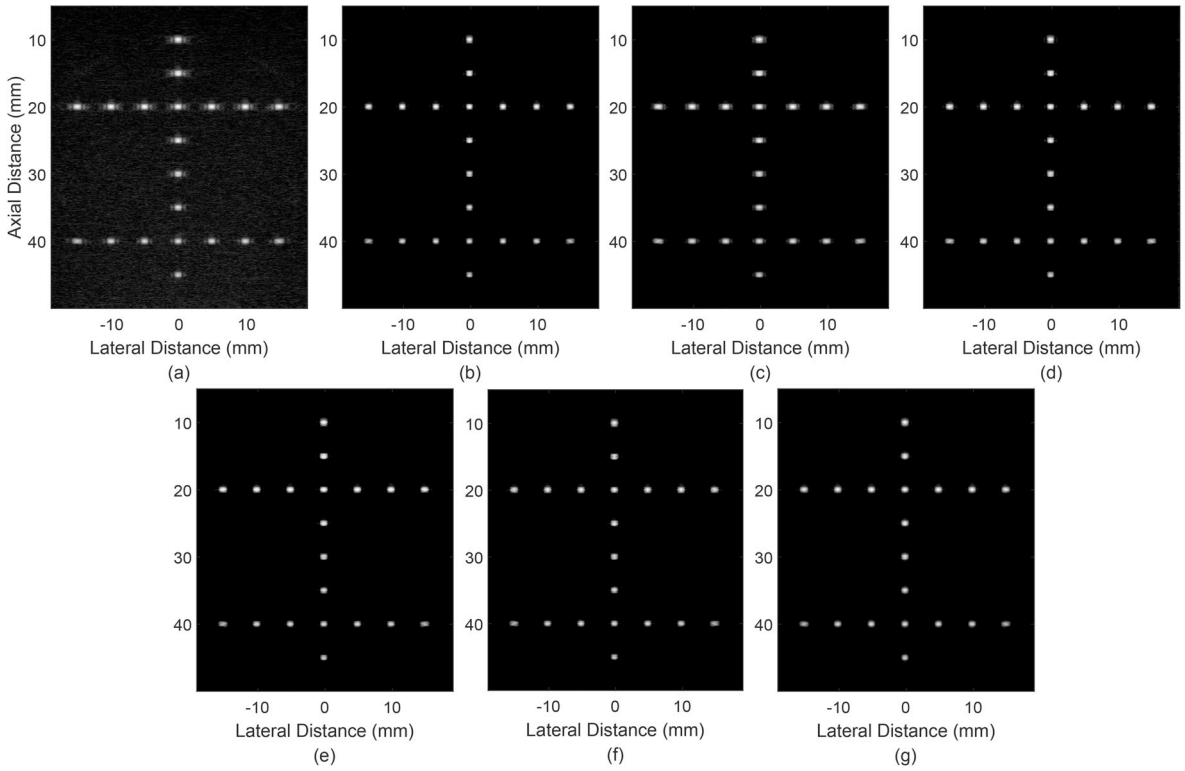

Fig. 2. Simulated point images acquired by different methods. (a) CPWC, (b) CF, (c) GCF, (d) scCF, (e) DCF, (f) ADCF, (g) SN-ADCF.

4. Results

4.1. Simulation result: point targets

Fig. 2 shows the simulated point images using different methods with a dynamic range of 60 dB. Fig. 2(b–g) have visually lower sidelobes and narrower mainlobes than Fig. 2(a), which indicates the performance of sidelobes suppression of the adaptive weighting methods. It can be observed that GCF has higher sidelobes compared with CF, scCF, DCF, ADCF and SN-ADCF. Fig. 3 gives the lateral variations of the point targets at (x, z) = (0 mm, 10 mm) and (x, z) = (0 mm, 45 mm) to show the performance of different methods in detail. It can be seen that the sidelobes of CF, scCF, DCF, ADCF and SN-ADCF are obviously lower than those of CPWC and GCF. Furthermore, for the near field region, SN-ADCF and ADCF show lower sidelobes than CF and scCF as shown in Fig. 3(a), while CF, scCF, DCF and ADCF have the almost equal sidelobe level at the deep region. It also can be seen that SN-ADCF shows the lowest sidelobes of all methods at 45 mm depth.

The two point targets are also selected for further quantitative measurement. Table 2 gives the lateral FWHM results. As shown, CF, GCF, scCF, DCF, ADCF and SN-ADCF all achieve improved resolution compared to CPWC. For both point targets, ADCF obtains the lowest lateral FWHM values, which shows FWHM improvements by 0.17 mm/0.01 mm than CF, 0.27 mm/0.14 mm than GCF and 0.26 mm/0.15 mm

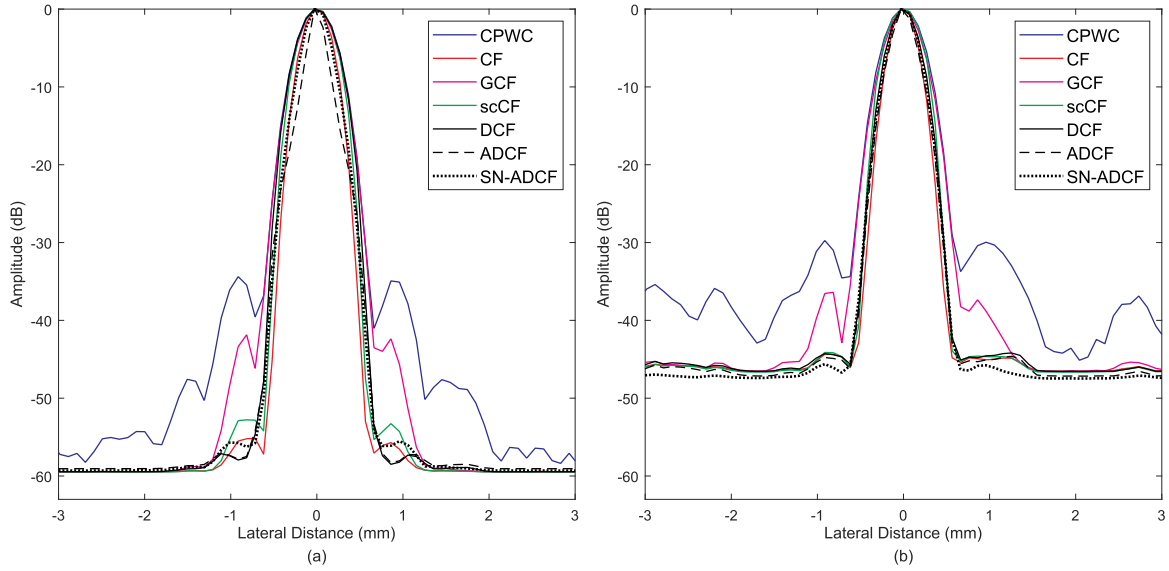

Fig. 3. The lateral variations of the two point targets in the simulated images. (a) (x, z) = (0 mm, 10 mm), (b) (x, z) = (0 mm, 45 mm).

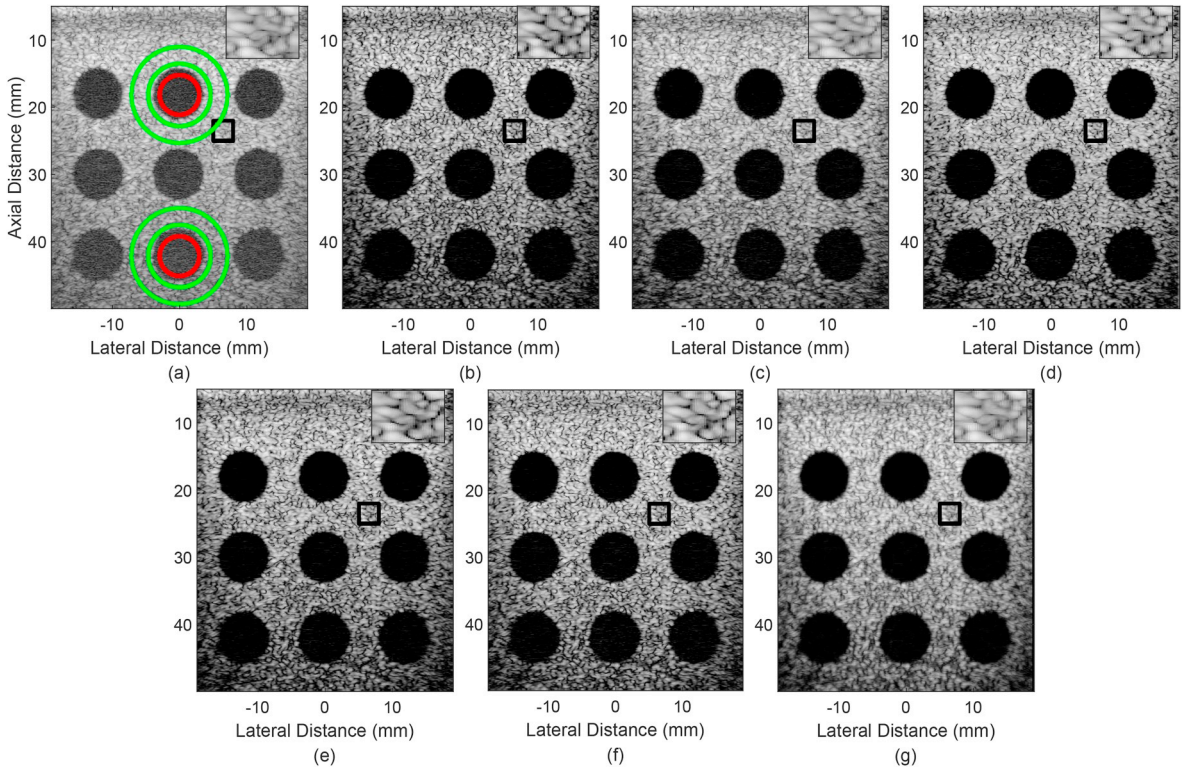

Fig. 4. Simulated cyst phantom images acqiured by different methods. (a) CPWC, (b) CF, (c) GCF, (d) scCF, (e) DCF, (f) ADCF, (g) SN-ADCF. The area in the red circle and between the two green circles indicates the lesion and scatter region, respectively, used for calculating CR, CNR and sSNR.

Table 2
Lateral FWHM values of the selected points in the simulated images formed by different methods.

Method	10 mm depth	45 mm depth
CPWC	0.54 mm	0.55 mm
CF	0.42 mm	0.37 mm
GCF	0.52 mm	0.50 mm
scCF	0.51 mm	0.51 mm
DCF	0.53 mm	0.43 mm
ADCF	0.25 mm	0.36 mm
SN-ADCF	0.38 mm	0.40 mm

than scCF. SN-ADCF have a little larger FWHM values than ADCF, which can provide FWHM improvements by 0.04 mm/−0.03 mm than CF, 0.14 mm/0.10 mm than GCF and 0.13 mm/0.11 mm than scCF. Also, it can be seen that the three proposed methods all provide improved resolution compared with GCF and scCF at 45 mm depth. For the axial FWHM, the adaptive weighting methods have similar values of about 0.40 mm to CPWC.

4.2. Simulation result: cyst targets

Simulated cyst images formed using different methods are displayed in Fig. 4 with a dynamic range of 60 dB. In Fig. 4(a), there is much noise in the cyst targets and background tissue. From Fig. 4(b)-(g), the CF, GCF, scCF, DCF, ADCF and SN-ADCF images show more detectable cysts, more distinct cyst edges and less noise than CPWC. However, the CF image shows slightly darken speckle background. It also can be observed from Fig. 4(e)–4(g) that the speckle background brightness gradually becomes higher, and the black-region artifacts gradually become fewer, which indicates the different performance of the proposed methods on speckle preservation. In Fig. 4, every image is displayed with a magnified view of a speckle region (enclosed by the black square) to clearly show the speckle quality and investigate the black-region artifacts. It is obvious that CF, DCF and ADCF show more visible black artifacts than CPWC, GCF, scCF and SN-ADCF. Though the speckle quality of SN-ADCF is still degraded compared with CPWC, the artifacts are compensated well by using the neighborhood average. Overall, SN-ADCF is observed to have a satisfying performance in reducing noise and preserving speckle in the proposed methods.

To illustrate the ability to suppress noise, the lateral cross sections of the two selected cyst targets from Fig. 4 are shown in Fig. 5. It can be seen that CF, scCF, DCF, ADCF and SN-ADCF show a more effective performance of noise and clutter reduction in the cysts than GCF. In the deep region, scCF and SN-ADCF have increased noise suppression compared with other methods as shown in Fig. 5(b). Two cyst targets are selected for further quantitative measurement. The CR, CNR and sSNR values are calculated based on formula 21, 22 and 23. Table 3 presents the results. CF, DCF, ADCF and SN-ADCF can offer CR improvements by more than 30 dB relative to CPWC for the two selected cysts. It can be seen that GCF shows the lowest CR but the highest CNR and sSNR values in the adaptive weighting methods. Compared with GCF, scCF can provide higher CR meanwhile obtaining similar CNR and sSNR. DCF, ADCF and SN-ADCF all obtain higher CNR and sSNR values than CF, which indicates that the proposed methods are superior to CF for preserving the speckle. On average, compared with CF, the CR, CNR and sSNR of SN-ADCF improved by 3.5%, 17% and 17%, respectively. SN-ADCF can achieve a CR enhancement by 4.67 dB/5.85 dB but degraded CNR and sSNR by 0.05/0.01 and 0.05/0.02 compared with GCF. It is also observed that SN-ADCF and scCF have almost equal CR, CNR and sSNR.

4.3. Experimental result: point phantom and cyst targets

Fig. 6 shows the experimental point phantom images obtained by different methods with a dynamic range of 60 dB. Similar to the simulation case, all adaptive weighting methods have better resolution performance than CPWC. However, DCF, ADCF and SN-ADCF show less

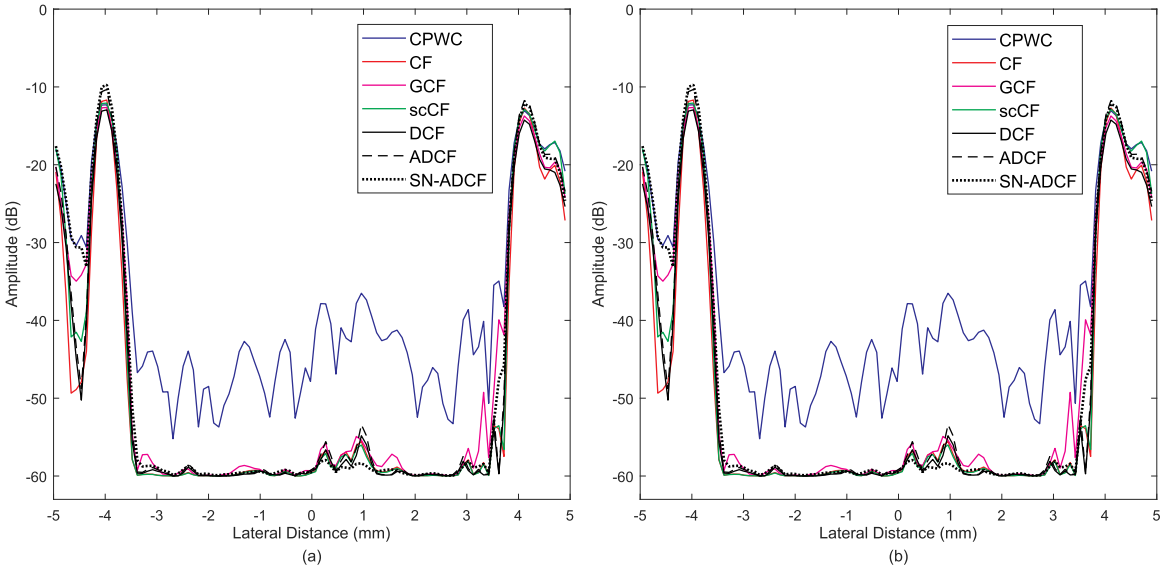

Fig. 5. Lateral cross sections of the anechoic cysts centred at (a) (x, z) = (0 mm, 18 mm) and (b) (x, z) = (0 mm, 42 mm) in the simulated cyst phantom images.

Table 3
CR, CNR and sSNR of the two simulated anechoic cysts for different methods.

Method	CR (dB)	CNR	sSNR
CPWC	31.68/17.76	1.56/1.29	1.60/1.49
CF	65.36/41.65	1.12/0.84	1.12/0.85
GCF	61.45/38.36	1.38/0.98	1.38/0.99
scCF	67.84/45.04	1.36/0.98	1.36/0.99
DCF	65.44/42.14	1.20/0.86	1.20/0.87
ADCF	63.54/41.82	1.22/0.87	1.22/0.87
SN-ADCF	66.12/44.21	1.33/0.97	1.33/0.97

sidelobe suppression over CPWC in the experiment compared with the simulation. Fig. 7 shows the lateral variations of two points located at (x, z) = (−0.5 mm, 8 mm) and (x, z) = (−0.2 mm, 48 mm) in the experimental images. CPWC has the widest mainlobes and highest sidelobes, while CF has the lowest sidelobes. In the deep region, CF, DCF, ADCF and SN-ADCF show better performance in sidelobes suppression than GCF and scCF as shown in Fig. 7(b). The statistical results of lateral FWHM are given in Table 4. Though ADCF has a little larger FWHM value than CF at 48 mm depth, it obtains the lowest lateral FWHM value (0.35 mm) in all methods at 8 mm depth. ADCF can achieve lateral FWHM improvements of 0.04 mm/−0.01 mm upon CF and 0.13 mm/0.06 mm upon GCF and scCF. The FWHM values of SN-

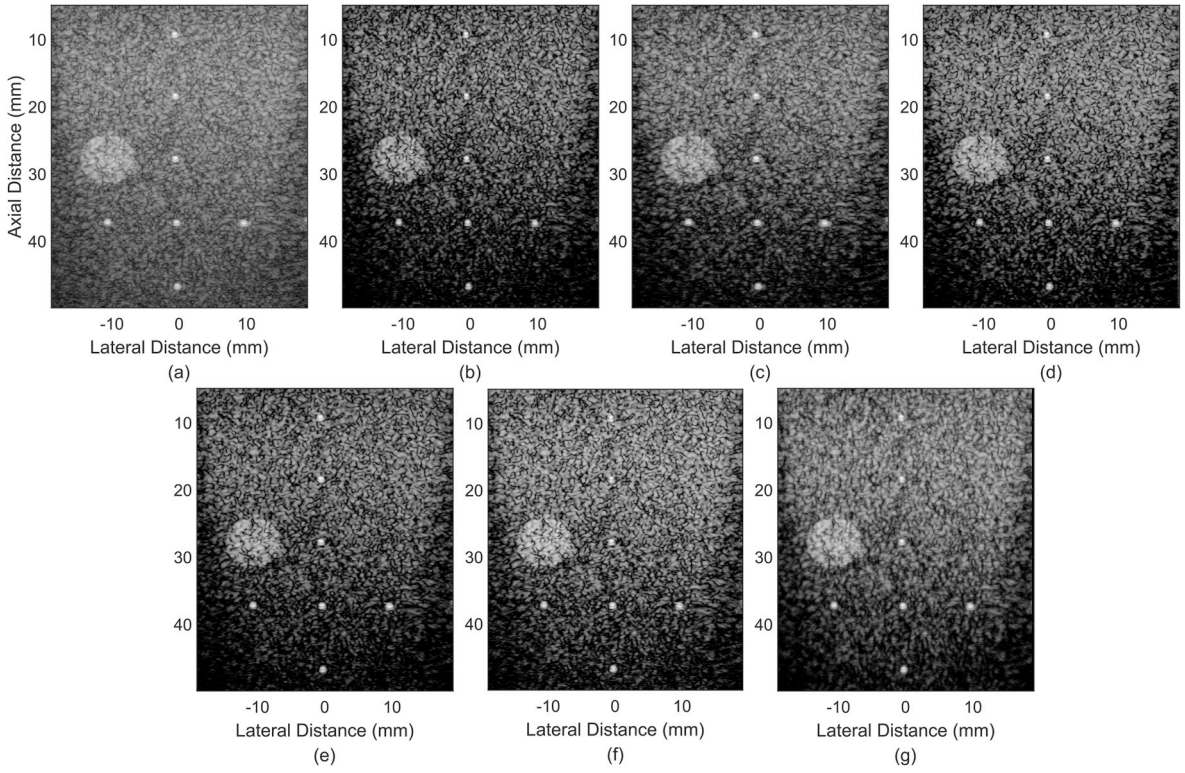

Fig. 6. Experimental point images acquired by different methods. (a) CPWC, (b) CF, (c) GCF, (d) scCF, (e) DCF, (f) ADCF, (g) SN-ADCF.

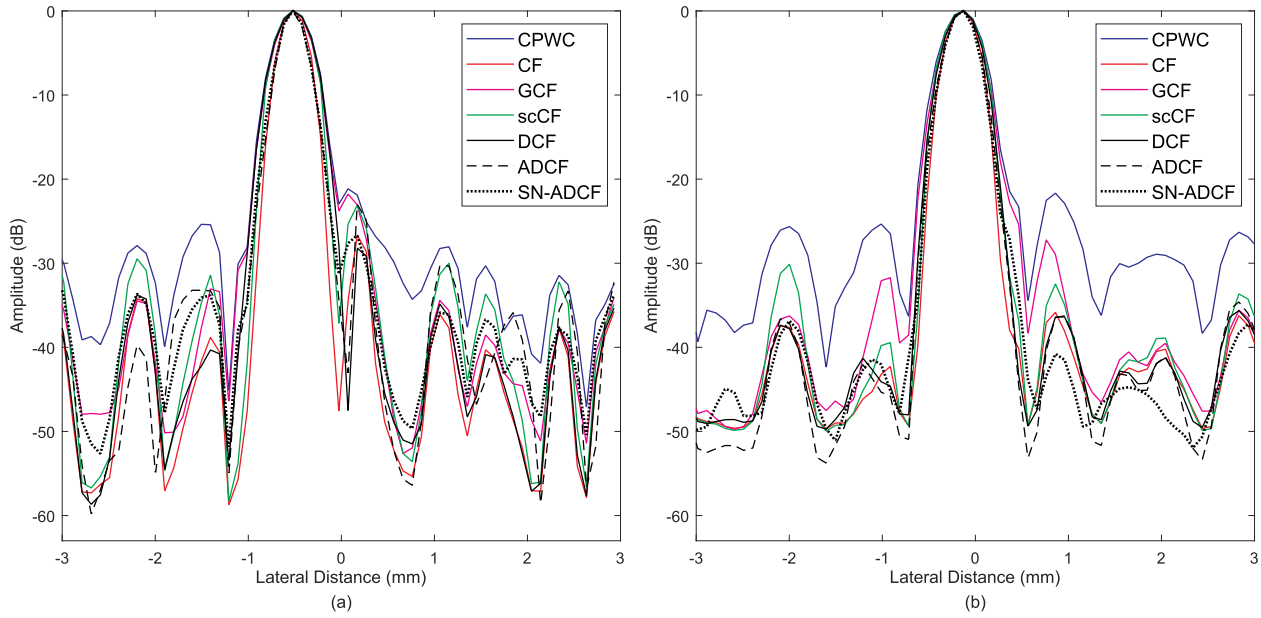

Fig. 7. The lateral variations of the two point targets in the experimental images. (a) (x, z) = (−0.5 mm, 8 mm), (b) (x, z) = (−0.5 mm 48 mm).

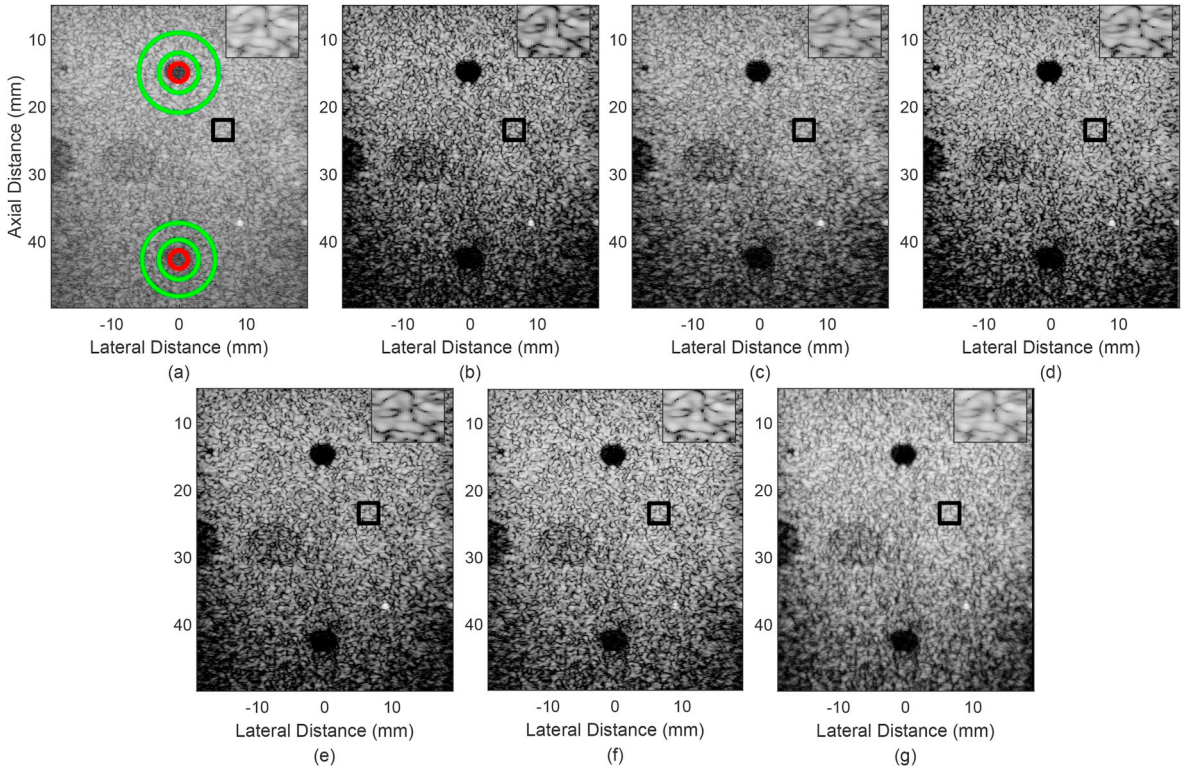

Fig. 8. Experimental cyst phantom images acquired by different methods. (a) CPWC, (b) CF, (c) GCF, (d) scCF, (e) DCF, (f) ADCF, (g) SN-ADCF. The area in the red circle and between the two green circles indicates the lesion and scatter region, respectively, used for calculating CR, CNR and sSNR.

ADCF have improvements of −0.02 mm/0.02 mm than CF, 0.11 mm/0.09 mm than GCF and scCF. In the experiment, the axial FWHM values of all methods are about 0.58 mm.

Experimental cyst images formed by different methods are displayed in Fig. 8 with a dynamic range of 60 dB. The adaptive weighting images show reduced noise inside the cysts, which leads to a contrast improvement. The dark artifacts are obvious in the CF image, particularly in the deep region. The magnified view of a speckle region (enclosed by the black square) is shown at the top of every experimental image. It can be seen that CPWC shows few black-region artifacts, while CF produces visible black-region artifacts. The speckle region of scCF, DCF and ADCF also can be observed detectable black-region artifacts, but fewer than CF. GCF, scCF and SN-ADCF have a good performance to protect speckle, whose images show relatively higher overall brightness and fewer artifacts than CF, DCF and ADCF. Also, for the deep region, the SN-ADCF image of Fig. 8(g) shows a higher speckle background brightness than Fig. 8(b–f).

The lateral cross sections of the experimental cysts are shown in Fig. 9. It can be seen from Fig. 9 that CF, scCF, DCF and SN-ADCF exhibit better performance of noise suppression for the cysts than GCF

Table 4
Lateral FWHM of the selected point targets in the experimental images.

Method	8 mm depth	48 mm depth
CPWC	0.51 mm	0.54 mm
CF	0.39 mm	0.43 mm
GCF	0.48 mm	0.50 mm
scCF	0.48 mm	0.51 mm
DCF	0.50 mm	0.48 mm
ADCF	0.35 mm	0.44 mm
SN-ADCF	0.37 mm	0.41 mm

Table 5
CR, CNR and sSNR of the two experimental cyst targets for different methods.

Method	CR (dB)	CNR	sSNR
CPWC	25.48/11.62	1.60/1.16	1.70/1.61
CF	52.18/30.22	1.10/0.69	1.11/0.71
GCF	48.55/26.55	1.38/0.83	1.39/0.87
scCF	54.97/34.62	1.33/0.72	1.33/0.74
DCF	53.89/33.42	1.19/0.77	1.19/0.79
ADCF	52.47/33.21	1.20/0.78	1.20/0.79
SN-ADCF	52.07/33.65	1.33/0.89	1.33/0.91

and ADCF. The CR, CNR and sSNR values of the experimental images are listed in Table 5. Although CPWC has the lowest CR, it achieves the largest CNR and sSNR. It can be seen that DCF, ADCF and SN-ADCF all obtain higher CR, CNR and sSNR than CF. The black-region artifacts lead to a large speckle variance in the CF image, which reflects the quantitative metrics to be low CNR and sSNR values. The scCF provides the highest CR, while it has lower CNR and sSNR than GCF. SN-ADCF shows better contrast and speckle quality than DCF and ADCF. Compared with CF, SN-ADCF can achieve an average CR improvement of 1.66 dB, CNR improvement of 0.22 and sSNR improvement of 0.21. SN-ADCF also shows higher CNR and sSNR than CF, GCF and scCF in the deep region, which indicates that SN-ADCF can provide better speckle quality for the deep region.

4.4. Experimental result: in-vivo images of the carotid artery

Compared to simulation and experimental phantom studies, the objects of *in-vivo* experiments have a more complex structure and the imaging results might be more affected by phase aberrations. In order to further validate the performance of the proposed methods, *in-vivo* data of a human carotid artery were used and the images beamformed by different methods are shown in Fig. 10 and Fig. 11 with a dynamic range of 60 dB. It can be seen that the noise inside the artery in the CF, GCF, scCF, DCF, ADCF and SN-ADCF images are significantly suppressed, which leads to the better visualized carotid. CPWC shows detailed anatomical structures but blurred artery boundary. In CF images, artery boundaries are more distinct compared to CPWC. However, the anatomical structures surrounding the carotid artery become less visible. It can be seen that GCF, scCF, ADCF and SN-ADCF can not only reduce noises inside the artery, while also better preserving the anatomical structures relative to CF and DCF.

The *in-vivo* images are also quantitatively evaluated using image quality metrics. In Fig. 10, there is a white circle for the carotid artery and a black box for the background region. The CR, CNR and sSNR results are presented in Table 6. Although the CF achieves increased CR, the CNR and sSNR values both decrease due to the increased speckle variance. SN-ADCF shows higher CR, CNR and sSNR values than CF and GCF. SN-ADCF can achieve CR enhancement by 1.59 dB, CNR enhancement by 0.03 and sSNR enhancement by 0.03 compared with GCF. For the *in-vivo* images, ADCF and SN-ADCF show higher CNR and sSNR values than other adaptive weighting methods.

5. Discussion

In this paper, we proposed modified CF methods for CPWC to improve the image quality. Simulation and experimental results show the different performance of the proposed methods in improving image resolution, contrast and speckle pattern compared with CF. The benefits of CF include lower sidelobes and higher contrast. However, CF usually gives rise to an over-suppression of the desired signal and introduces dark artifacts into the speckle region [16]. The speckle pattern might be badly damaged in CF images [37]. Furthermore, in consideration of the influence of the angular coherence and angular difference on the CPWC image quality, DCF, ADCF and SN-ADCF are proposed to overcome the shortcomings of CF and to weight CPWC for high-quality images. We compared the proposed methods with CF, GCF and scCF to validate their performance. As a whole, DCF can achieve improved contrast and speckle quality relative to CF. ADCF obtains a resolution improvement upon CF, GCF and scCF. SN-ADCF has the best performance of contrast improvement and speckle preservation in the proposed methods. SN-

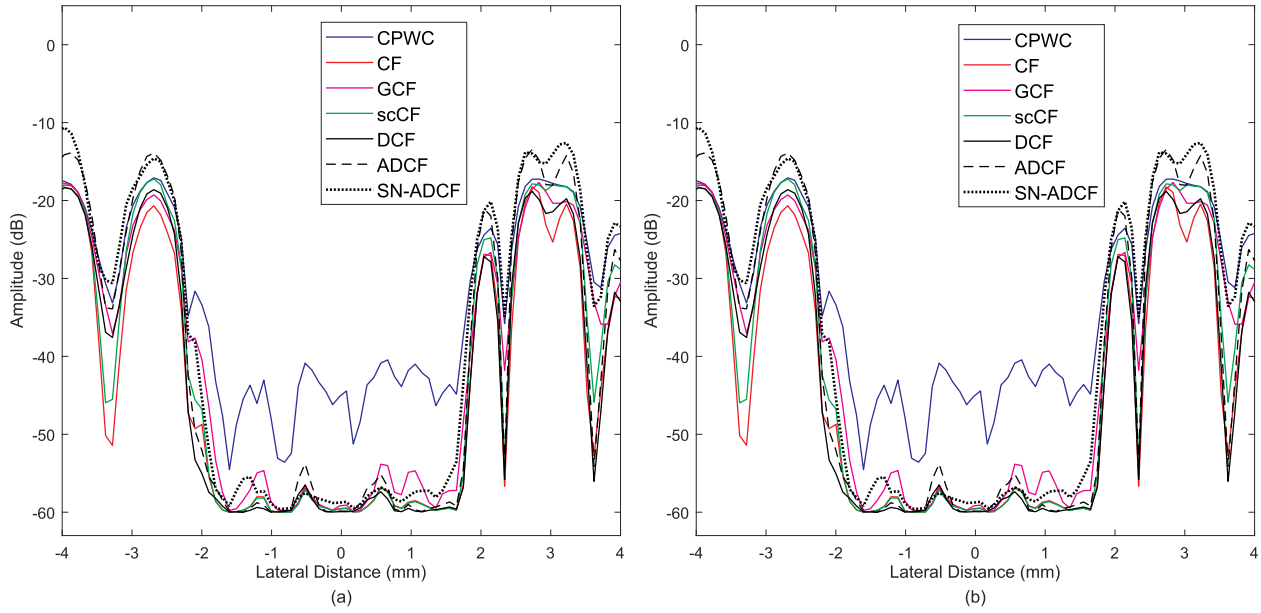

Fig. 9. Lateral cross sections of the anechoic cysts centred at (a) (x, z) = (0 mm, 15 mm) and (b) (x, z) = (0 mm, 43 mm) in the experimental cyst phantom images.

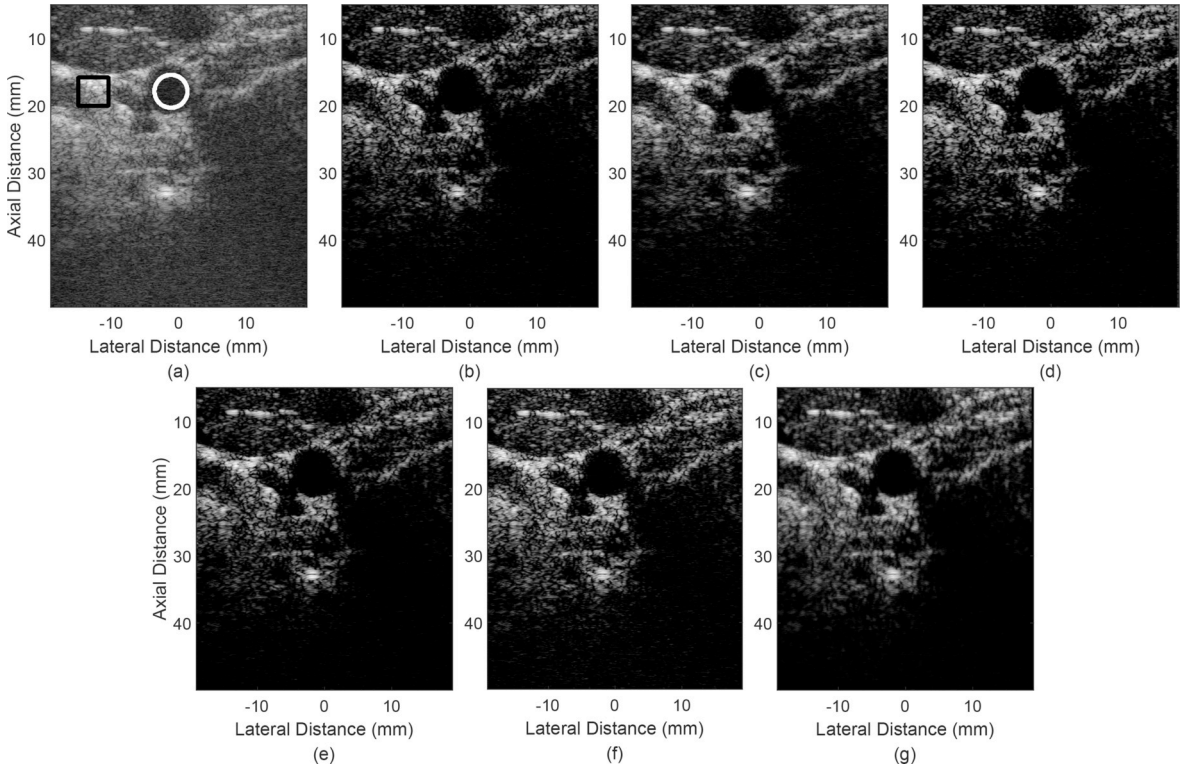

Fig. 10. *In-vivo* transverse cross images of the carotid artery acquired by different methods. (a) CPWC, (b) CF, (c) GCF, (d) scCF, (e) DCF, (f) ADCF, (g) SN-ADCF. The area in the white circle and black rectangle indicates the lesion and scatter region, respectively, used for calculating CR, CNR and sSNR.

ADCF can achieve better resolution and contrast than GCF. Compared with scCF, SN-ADCF provides a little lower CR, but with improved resolution and similar CNR and sSNR.

As shown in Figs. 3 and 7, DCF, ADCF and SN-ADCF show suppressed sidelobes compared with GCF and scCF. To better show the effect of different beamformers on sidelobes, images of the simulated point located at (x,z) = (0 mm, 10 mm) with a dynamic range of 80 dB are shown in Fig. 12. It can also be seen that DCF, ADCF and SN-ADCF

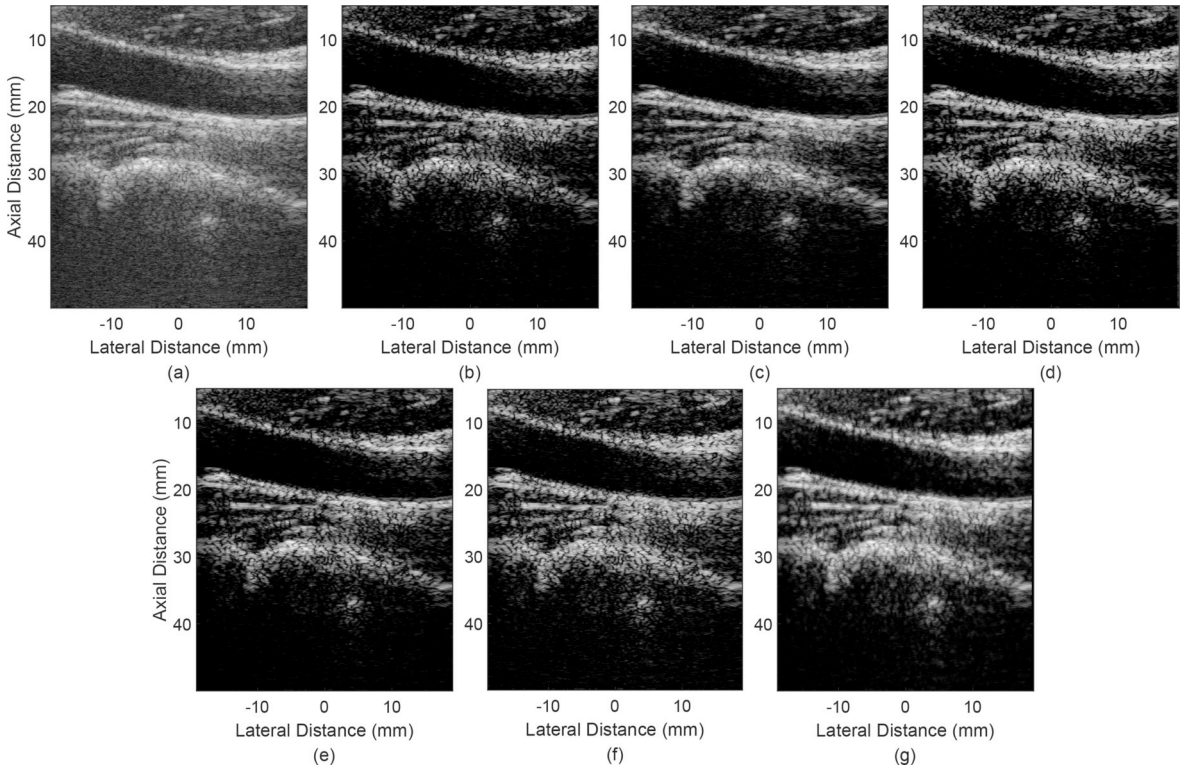

Fig. 11. *In-vivo* longitudinal sectional images of the carotid artery acquired by different methods. (a) CPWC, (b) CF, (c) GCF, (d) scCF, (e) DCF, (f) ADCF, (g) SN-ADCF.

Table 6
CR, CNR and sSNR of the carotid artery images for different methods.

Method	CR (dB)	CNR	sSNR
CPWC	34.30	0.77	0.78
CF	60.39	0.55	0.55
GCF	59.11	0.64	0.64
scCF	64.86	0.63	0.63
DCF	63.02	0.56	0.56
ADCF	57.82	0.67	0.67
SN-ADCF	60.70	0.67	0.67

are more effective at suppressing sidelobes than GCF and scCF. From Tables 2 and 4, DCF has a weak resolution performance, while ADCF shows the lowest FWHM of all methods. For DCF, we introduce a parameter δ which is related to the normalized standard deviation to dynamically determine the effective plane-wave number. Then, based on the plane-wave number, several PWI results obtained with small transmitting angular difference are selected to calculate the coherence factor. This can be regarded as using a decreased number of plane waves to obtain CF, which results in a declined estimation of signal coherence. Therefore, DCF shows weak resolution performance. ADCF utilizes the parameter δ equal to $(1-\sigma')^2$ to multiply DCF and adjust its performance. For point targets or hyper-echoic tissues, the normalized standard deviation of echo signals is small. According to Eq. (13), the δ value will be close to 1. Thus, the corresponding ADCF value will approach to the DCF value. That means that ADCF will have a weak ability to narrow mainlobes. However, due to square operation, ADCF can achieve lower FWHM values. We also observed that SN-ADCF has larger lateral FWHM values than ADCF, which results from the application of the 2-dimensional moving average filter.

From Figs. 4 and 8, we see that the proposed methods can efficiently reduce the noises in cysts and speckle background. There is much uncorrelated clutter and noise in the echo signals from the cysts and background tissues. The signals with clutter and noise are less coherent, contributing to small weighting factor values. Therefore, adaptive weighting methods are able to suppress undesired signals and obtain significantly improved contrast relative to CPWC. Echoes from individual interrogated reflectors have different SNR levels resulting from different amounts of noise and interference related to the scattering surroundings of the reflectors, which leads to the weighting factor varying greatly at each image pixel [38]. CF is susceptible to noise. Therefore, it is usually not expected to work well in low SNR. For example, CF usually underestimates speckle magnitude and decreases the image intensity. Black-region artifacts are visible in the images of CF, particularly in the deep region with a low SNR. The DCF values are obtained with high angular coherence signals. Thus, it can estimate the signal coherence more accurately. As seen in the images of DCF, these artifacts are relieved, and improved speckle is obtained with a low speckle variance. As a result, DCF can provide higher CR, CNR and sSNR than CF. For ADCF, further less black-region artifacts and improved speckle quality can be observed in Figs. 4 and 8. The parameter δ can reflect the signal incoherence. Therefore, ADCF using δ can adjust the weight of coherent energy in CF formulation to maintain the desired signal level. The weighting factor variations of ADCF are alleviated leading to reduced speckle variations. However, this also causes a slightly declined noise suppression in cysts. Thus the CR values of ADCF are a little smaller than DCF and CF. SN-ADCF uses the square neighborhood average which can be seen as a 2-dimensional moving average filter [30]. It can reduce noise and yield homogeneous speckle pattern by smoothing. Consequently, SN-ADCF achieves higher contrast and better speckle quality than DCF and ADCF.

The *in-vivo* images of the carotid artery formed by DCF-based methods show that the noise inside the carotid artery is effectively removed and the carotid artery boundary is distinct, which also confirms the contrast enhancement performance of the proposed methods. Table 6 indicates that SN-ADCF can simultaneously obtain satisfying CR, CNR and sSNR, which is in correspondence with the simulation and experimental phantom results. It should be noted that the speckle quality of SN-ADCF is improved at the cost of resolution degradation due to the square neighborhood average. DCF shows similar CNR and sSNR with CF. However, ADCF and SN-ADCF obtain visibly higher CNR and sSNR values, which is potentially beneficial to the diagnostic information typically provided by the presence of speckle. Therefore, ADCF and SN-ADCF have better performance for *in-vivo* imaging and are likely better suited to clinical applications.

As the number of compounding angles could affect the beamforming performance, all methods were performed on the experimental datasets to evaluate the performance parameters with several compounding numbers ranging from 5 to 75. The angular range was chosen as $[-\alpha_{max}, +\alpha_{max}]$ with a fixed increment of 0.43°. For instance, when the compounding number was five, the angular range was [0.86°, − 0.86°] and five angles (i.e., − 0.86°, − 0.43°, 0°, 0.43°, 0.86°) were used to create a compounded image. The quantitative results of lateral FWHM, CR, CNR and sSNR are shown in Figs. 13 and 14. It can be seen that the lateral FWHM and CR improve when increasing the number of plane waves, while CNR and sSNR degrade as the compounding number increases. Overall, ADCF and SN-ADCF show better performance of lateral resolution than other methods. Compared with CF, the proposed methods show similar contrast performance and improved speckle pattern. It can also be observed that the CNR and sSNR provided by SN-ADCF are higher than those of DCF and ADCF but lower than GCF and scCF. SN-ADCF can achieve a better performance of lateral resolution than scCF and GCF. The CR values of SN-ADCF are also higher than those of GCF. Moreover, for the deep region, it can be seen that SN-ADCF shows similar CNR and sSNR with GCF and scCF. As shown in Fig. 14(c) and (d), when the compounding number is greater than 60, SN-ADCF can provide higher CNR and sSNR than GCF and scCF. Therefore, SN-ADCF can obtain a good trade-off between contrast and resolution, meanwhile maintaining a good speckle quality. Also, using a different number of plane waves for compounding, the proposed methods have similar improvements when compared with the other methods.

Because the normalized standard deviation is related to noise intensity, noise with various intensity was added to datasets to further illustrate the robustness of the proposed methods. In this paper, we used the experimental phantom dataset to quantitatively measure image quality metrics with the SNR of the added Gaussian distribute noise varying from 0 dB to 20 dB. The experimental point target located

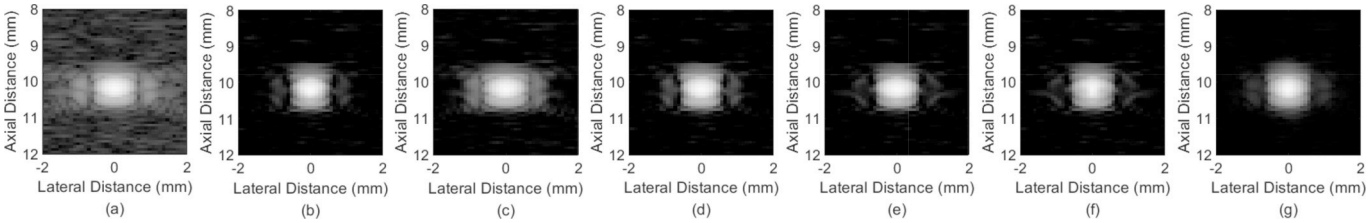

Fig. 12. Zoomed B-mode images for the simulated point target at 10 mm depth using different beamformers. (a) CPWC, (b) CF, (c) GCF, (d) scCF, (e) DCF, (f) ADCF, (g) SN-ADCF. All images are displayed with a dynamic range of 80 dB.

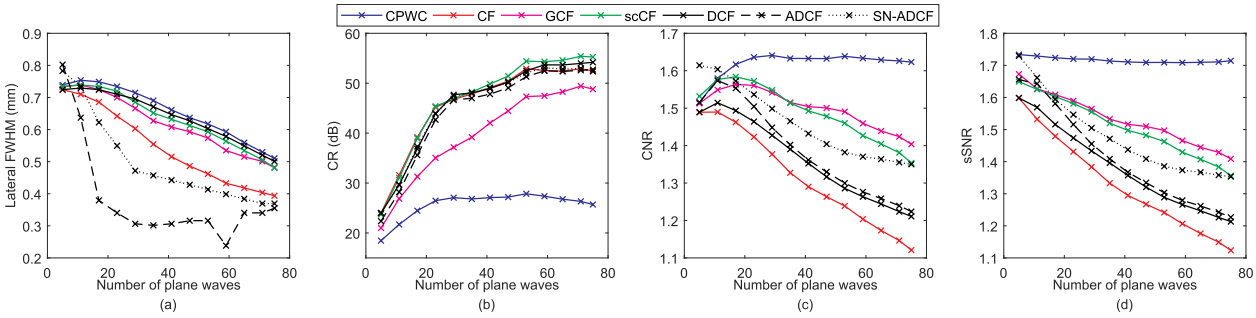

Fig. 13. Effect of the number of plane waves on the performance parameters in experiment with the point target located at (x, z) = (0 mm, 8 mm) and the cyst at 15 mm depth. (a) Lateral FWHM, (b) CR, (c) CNR, (d) sSNR.

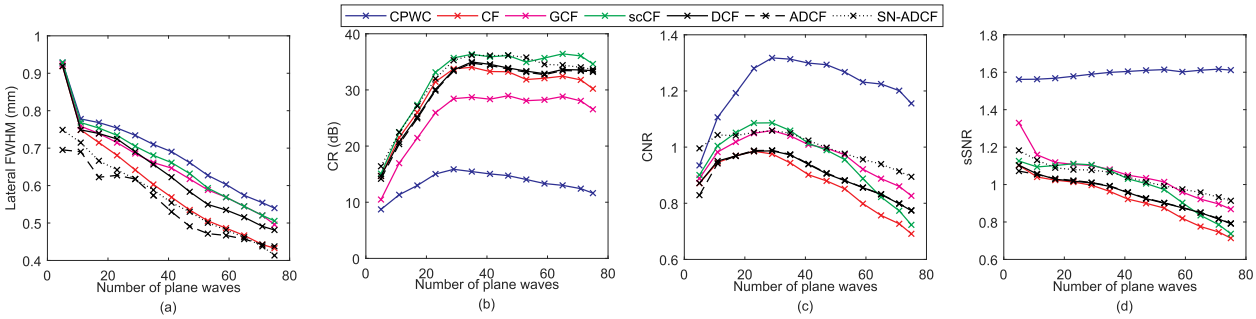

Fig. 14. Effect of the number of plane waves on the performance parameters in experiment with the point target located at (x, z) = (0 mm, 48 mm) and the cyst at 43 mm depth. (a) Lateral FWHM, (b) CR, (c) CNR, (d) sSNR.

at (x, z) = (−0.5 mm, 8 mm) was selected to evaluate the lateral FWHM and the experimental cyst target at depth 15 mm was chosen to calculate the CR, CNR and sSNR values. Results are shown in Fig. 15. It can be observed that decreasing the added noise intensity results in contrast improvement. However, the lateral FWHM, CNR and sSNR vary slightly as the added noise decreases. Basically, ADCF and SN-ADCF obtain obviously lower lateral FWHM values than other methods, while scCF achieves the highest CR values of all methods. It can be observed from Fig. 15 that the proposed methods can provide almost as high contrast as CF and scCF as the noise intensity varies. SN-ADCF performs well in the high-noise environment, which provides higher CNR and sSNR when the SNR of the added Gaussian distribute noise is 0 dB. As a whole, the performance of the proposed methods is consistent with the previous analysis in this paper and is robust when the noise intensity is varying. Therefore, it can be concluded that DCF-based methods can maintain a stable performance when the noise intensity varies.

The computational load, computational complexity and runtime of different methods are calculated to evaluate the computational efficiency. A floating-point operation (FLOP) is assumed to be either a complex multiplication or a complex summation, and it is used to evaluate the computational load. The runtime of different beamformers is recorded on the PC with Intel Core i5-7500 CPU running at 3.40 GHz and RAM 16 GB using the experimental datasets with 75 plane waves. The number of compounding angles is $2N + 1$. M_0 and R are respectively defined in Eq. (7) and Eq. (14), while S and L are defined in Eq. (19). CF and GCF has a computational complexity of $[O(2N)]$ and $[O((2N + 1)\log_2(2N + 1))]$, respectively. CF requires $2(2N + 1)$ multiplications and $(2N + 1)$ additions. GCF requires a Fast Fourier Transformation (FFT) operation $[O((2N + 1)\log_2(2N + 1))]$, $2N + 1$ multiplications and $2N + 1$ additions [30,39]. In the formulation of scCF Eq. (9), the calculation of the weight $\eta(SNR)$ requires FFT operation and local SNRs average. Therefore, the computation of scCF is more complex than CF and GCF [26]. The corresponding runtime of CF, GCF and scCF are 2.52 s, 8.89 s and 17.03 s. The computational complexities of DCF and ADCF primarily result from the mean operator, standard deviation operator and coherence factor calculation, which requires about $(2N + 2R + 9)$ multiplications and $(6N + 4R + 2)$ additions. Due to the smoothing, SN-ADCF requires an additional $(2S + 1)(2L + 1)$ additions compared with ADCF. CF, DCF, ADCF and SN-ADCF require $(6N + 4)$, $(8N + 6R + 11)$, $(8N + 6R + 12)$ and $(8N + 6R + (2S + 1)(2L + 1) + 12)$ FLOPs, respectively. The recorded runtimes for DCF, ADCF and SN-ADCF are 11.08 s, 11.34 s and 13.09 s, respectively. It can be seen that the proposed methods require about 4-fold runtime of CF. Besides, the proposed methods are more computationally efficient than scCF but less efficient than GCF.

6. Conclusion

The dynamic coherence factor based methods are proposed for CPWC in this study to modify CF and improve the image quality. The proposed methods were evaluated on both simulated and experimental data and compared with CF, GCF and scCF methods. We show that the proposed methods can achieve higher speckle quality than CF. DCF obtains an improved contrast and speckle quality compared with CF. ADCF has a better resolution performance than CF, GCF and scCF. SN-ADCF can further suppress noise and preserve speckle, which shows higher contrast than CF and GCF meanwhile maintaining a good speckle pattern. Observing that SN-ADCF can provide the best speckle quality of the proposed methods and a good trade-off between resolution and contrast, SN-ADCF is recommended to be applied to CPWC. The proposed methods also show good robustness with the variation of noise intensity. Furthermore, due to a low computational complexity required, the proposed methods have potential applications in ultrafast imaging for high-quality images.

Conflicts of interest

We declare that we have no financial and personal relationships with other people or organizations. None of the authors have a conflicts of interest.

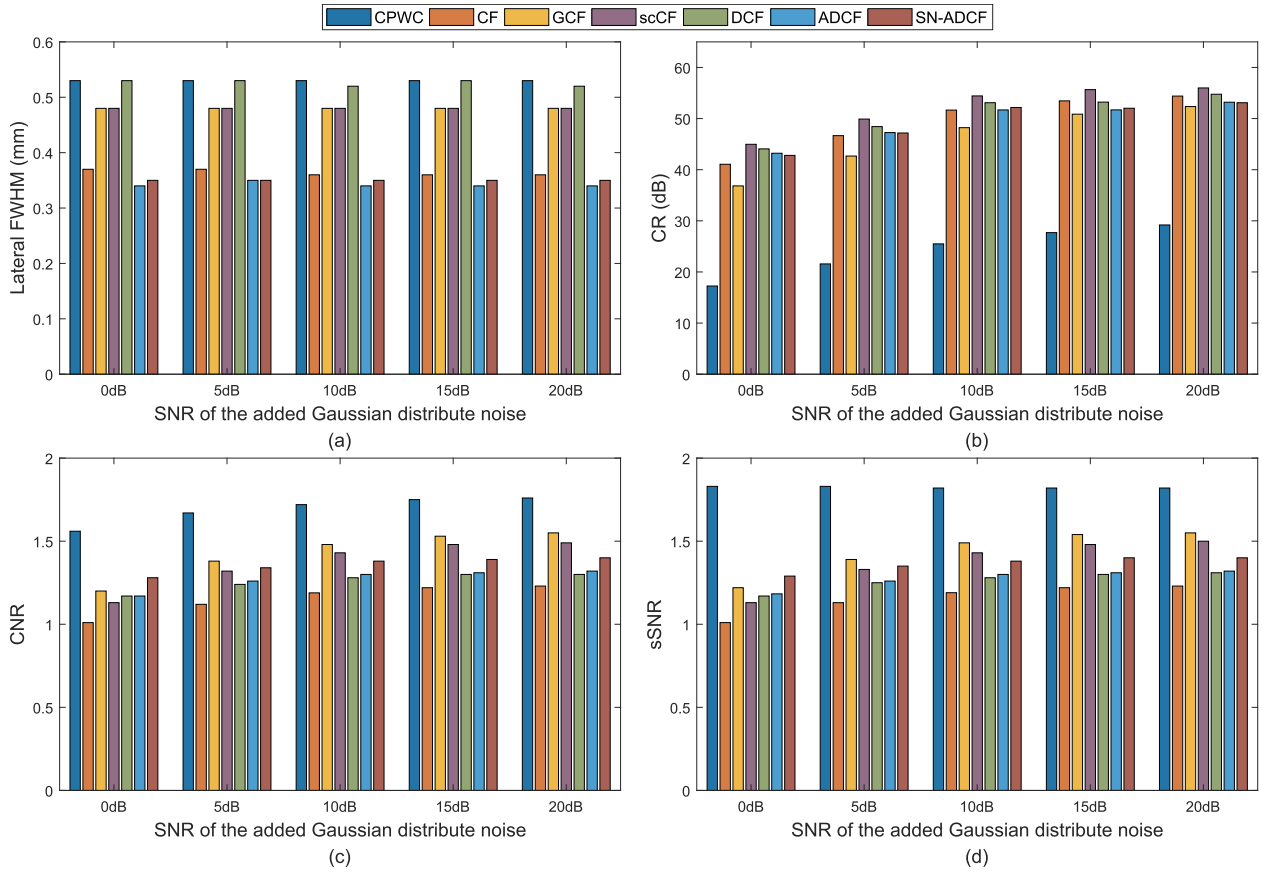

Fig. 15. Quantitative estimate for experimental image quality with different SNR of the added Gaussian distribute noise. (a) Lateral FWHM, (b) CR, (c) CNR, (d) sSNR.

Acknowledgement

This work was supported by the National Natural Science Foundation of China (61201060) and (61172037).

References

[1] O. Couture, M. Fink, M. Tanter, Ultrasound contrast plane wave imaging, IEEE Trans. Ultrason. Ferroelectr. Freq. Control 59 (2012) 2676–2683.
[2] M. Tanter, M. Fink, Ultrafast imaging in biomedical ultrasound, IEEE Trans. Ultrason. Ferroelectr. Freq. Control 61 (2014) 102–119.
[3] I.K. Holfort, F. Gran, J.A. Jensen, Broadband minimum variance beamforming for ultrasound imaging, IEEE Trans. Ultrason. Ferroelectr. Freq. Control 56 (2009) 314–325.
[4] J. Zhao, Y. Wang, J. Yu, W. Guo, T. Li, Y.-P. Zheng, Subarray coherence based postfilter for eigenspace based minimum variance beamformer in ultrasound plane-wave imaging, Ultrasonics 65 (2016) 23–33.
[5] J.-Y. Lu, 2D and 3D high frame rate imaging with limited diffraction beams, IEEE Trans. Ultrason. Ferroelectr. Freq. Control 44 (1997) 839–856.
[6] J.-Y. Lu, Experimental study of high frame rate imaging with limited diffraction beams, IEEE Trans. Ultrason. Ferroelectr. Freq. Control 45 (1998) 84–97.
[7] J. Cheng, J. yu Lu, Extended high-frame rate imaging method with limited-diffraction beams, IEEE Trans. Ultrason. Ferroelectr. Freq. Control 53 (2006) 880–899.
[8] G. Montaldo, M. Tanter, J. Bercoff, N. Benech, M. Fink, Coherent plane-wave compounding for very high frame rate ultrasonography and transient elastography, IEEE Trans. Ultrason. Ferroelectr. Freq. Control 56 (2009) 489–506.
[9] Y. Zhang, Y. Guo, W. Lee, Ultrafast ultrasound imaging using combined transmissions with cross-coherence-based reconstruction, IEEE Trans. Med. Imaging 37 (2018) 337–348.
[10] B. Osmanski, M. Pernot, G. Montaldo, A. Bel, E. Messas, M. Tanter, Ultrafast Doppler imaging of blood flow dynamics in the myocardium, IEEE Trans. Med. Imaging 31 (2012) 1661–1668.
[11] L. He, Y. Guo, W.N. Lee, Systematic performance evaluation of a cross-correlation-based ultrasound strain imaging method, Ultrasound Med. Biol. 42 (2016) 2436–2456.
[12] P. Song, H. Zhao, A. Manduca, M.W. Urban, J.F. Greenleaf, S. Chen, Comb-push ultrasound shear elastography (cuse): a novel method for two-dimensional shear elasticity imaging of soft tissues, IEEE Trans. Med. Imaging 31 (2012) 1821–1832.
[13] S. Pengfei, M.W. Urban, M. Armando, Z. Heng, J.F. Greenleaf, C. Shigao, Comb-push ultrasound shear elastography (cuse) with various ultrasound push beams, IEEE Trans. Med. Imaging 32 (2013) 1435–1447.
[14] Y. Xue, G. Yuexin, H. Sheng-Min, L. Meng-Lin, L. Wei-Ning, Beamforming effects on generalized nakagami imaging, Phys. Med. Biol. 60 (2015) 7513–7531.
[15] K. Hollman, K. Rigby, M. O'Donnell, Coherence factor of speckle from a multi-row probe, Ultrasonics Symposium, 1999, Proceedings. 1999 IEEE, 2 1999, pp. 1257–1260.
[16] Y. Qi, Y. Wang, W. Guo, Joint subarray coherence and minimum variance beamformer for multitransmission ultrasound imaging modalities, IEEE Trans. Ultrason. Ferroelectr. Freq. Control 65 (2018) 1600–1617.
[17] C.-I.C. Nilsen, S. Holm, Wiener beamforming and the coherence factor in ultrasound imaging, IEEE Trans. Ultrason. Ferroelectr. Freq. Control 57 (2010) 1329–1346.
[18] P.-C. Li, M.-L. Li, Adaptive imaging using the generalized coherence factor, IEEE Trans. Ultrason. Ferroelectr. Freq. Control 50 (2003) 128–141.
[19] J. Camacho, M. Parrilla, C. Fritsch, Phase coherence imaging, IEEE Trans. Ultrason. Ferroelectr. Freq. Control 56 (2009) 958–974.
[20] Y.H. Wang, P.C. Li, SNR-dependent coherence-based adaptive imaging for high-frame-rate ultrasonic and photoacoustic imaging, IEEE Trans. Ultrason. Ferroelectr. Freq. Control 61 (2014) 1419–1432.
[21] W. Guo, Y. Wang, J. Yu, Ultrasound harmonic enhanced imaging using eigenspace-based coherence factor, Ultrasonics 72 (2016) 106–116.
[22] M. Mozaffarzadeh, Y. Yan, M. Mehrmohammadi, B. Makkiabadi, Enhanced linear-array photoacoustic beamforming using modified coherence factor, J. Biomed. Opt. 23 (2018) 026005–1–10.
[23] Y.L. Li, J.J. Dahl, Angular coherence in ultrasound imaging: theory and applications, J. Acoust. Soc. Am. 141 (2017) 1582–1594.
[24] W. Guo, Y. Wang, G. Wu, J. Yu, Sidelobe reduction for plane wave compounding with a limited frame number, Biomed. Eng. Online 17 (2018) 94.
[25] S. Bae, T.-K. Song, Methods for grating lobe suppression in ultrasound plane wave imaging, Appl. Sci. 8 (2018).
[26] A.J. Zimbico, D.W. Granado, F.K. Schneider, J.M. Maia, A.A. Assef, N. Schiefler, E.T. Costa, Eigenspace generalized sidelobe canceller combined with snr dependent coherence factor for plane wave imaging, Biomed. Eng. Online 17 (2018) 109.
[27] B. Du, X. Wu, H. Zheng, S. Fang, M. Lu, R. Mao, Coherence plane-wave compounding with angle coherence factor for ultrafast ultrasound imaging, 40th Annual International Conference of the IEEE Engineering in Medicine and Biology Society, EMBC), 2018, pp. 907–910.
[28] H. Liebgott, A. Rodriguez-Molares, F. Cervenansky, J. Jensen, O. Bernard, Plane-wave imaging challenge in medical ultrasound, Ultrasonics Symposium (IUS), IEEE

International, 2016, pp. 1–4 2016.
[29] Plane-wave imaging challenge in medical ultrasound (PICMUS), IEEE IUS 2016, Tours, France, 2016 https://www.creatis.insa-lyon.fr/Challenge/IEEE_IUS_2016/.
[30] Y. Wang, C. Zheng, H. Peng, Q. Chen, An adaptive beamforming method for ultrasound imaging based on the mean-to-standard-deviation factor, Ultrasonics 90 (2018) 32–41.
[31] J.A. Jensen, N.B. Svendsen, Calculation of pressure fields from arbitrarily shaped, apodized, and excited ultrasound transducers, IEEE Trans. Ultrason. Ferroelectr. Freq. Control 39 (1992) 262–267.
[32] J.A. Jensen, Field: a program for simulating ultrasound systems, Med. Biol. Eng. Comput. 34 (1996) 351–353.
[33] J. Zhao, Y. Wang, J. Yu, W. Guo, S. Zhang, S. Aliabadi, Short-lag spatial coherence ultrasound imaging with adaptive synthetic transmit aperture focusing, Ultrason. Imag. 39 (2017) 224–239.
[34] X. Zeng, C. Chen, Y. Wang, Eigenspace-based minimum variance beamformer combined with wiener postfilter for medical ultrasound imaging, Ultrasonics 52 (2012) 996–1004.
[35] M.A. Lediju, G.E. Trahey, B.C. Byram, J.J. Dahl, Short-lag spatial coherence of backscattered echoes: imaging characteristics, IEEE Trans. Ultrason. Ferroelectr. Freq. Control 58 (2011) 1377–1388.
[36] Y. Wang, C. Zheng, H. Peng, X. Chen, Short-lag spatial coherence combined with eigenspace-based minimum variance beamformer for synthetic aperture ultrasound imaging, Comput. Biol. Med. 91 (2017) 267–276.
[37] S.M. Hverven, O.M.H. Rindal, A. Rodriguez-Molares, A. Austeng, The influence of speckle statistics on contrast metrics in ultrasound imaging, IEEE International Ultrasonics Symposium (IUS), 2017, pp. 1–4.
[38] M. Xu, X. Yang, M. Ding, M. Yuchi, Spatio-temporally smoothed coherence factor for ultrasound imaging, IEEE Trans. Ultrason. Ferroelectr. Freq. Control 61 (2014) 182–190.
[39] Y. Wang, C. Zheng, H. Peng, C. Zhang, Coherent plane-wave compounding based on normalized autocorrelation factor, IEEE Access 6 (2018) 36927–36938.